

Large Segmented UV-Optical Space Telescope Using a Hybrid Sensor Active Control (HSAC) Architecture

Lee D. Feinberg, Bruce Dean, Tupper Hyde, Bill Oegerle, Matthew R. Bolcar, J. Scott Smith
Goddard Space Flight Center, Greenbelt, MD 20771

ABSTRACT

Future large UV-optical space telescopes offer new and exciting windows of scientific parameter space. These telescopes can be placed at L2 and borrow heavily from the James Webb Space Telescope (JWST) heritage. For example, they can have similar deployment schemes, hexagonal mirrors, and use Wavefront Sensing and Control (WFSC) technologies developed for JWST. However, a UV-optical telescope requires a 4x improvement in wavefront quality over JWST to be diffraction-limited at 500 nm. Achieving this tolerance would be difficult using a passive thermal architecture such as the one employed on JWST. To solve this problem, our team has developed a novel Hybrid Sensor Active Control (HSAC) architecture that provides a cost effective approach to building a segmented UV-optical space telescope. In this paper, we show the application of this architecture to the ST-2020 mission concept and summarize the technology development requirements.

Keywords: ATLAST, ST-2020, Wavefront Sensing and Control, WFSC, Fine Guidance Sensor, Hybrid, Segmented Mirrors

INTRODUCTION

With the completion of the final servicing mission to the Hubble Space Telescope (HST) and the development of the James Webb Space Telescope, the astronomical community has begun planning the next great observatory. An important mission study for the next generation UV-optical observatory was the Advanced Technology Large-Aperture Space Telescope (ATLAST). ATLAST includes 3 primary mission concept optionsⁱ. The first two mission concepts include both an 8-m monolith primary telescope and a 16-m telescope and take advantage of plans to develop the Ares V launch vehicle, which would have considerable launch mass capabilities. Our team at GSFC was tasked to develop the third mission concept, named ST-2020, which leverages the architecture of the JWST and can be launched on an Enhanced Expendable Launch Vehicle (EELV). Our team had to consider the key science objectives of this mission, which include extra-solar planet studies as well as wide field-of-view (WFOV) UV-Optical imaging and spectroscopy. To accommodate a deployable and therefore segmented telescope, our team investigated two options for extra-solar studies: an external occulter that is compatible with a segmented telescope, and a Visible Nulling Coronagraph (VNC) that actually takes advantage of the segmented architecture by using a deformable, hexagonal mirror array for internal alignment optimizations. These two configurations minimize the requirements on the optical telescope assembly (OTA) necessitating only modest improvements in mirror technology over what was demonstrated by the Advanced Mirror System Demonstrator (AMSD)ⁱⁱ.

The size and mass restrictions of the EELV imply that the telescope would have mass requirements of about half that of the 8-meter monolith concept, and would rely on a deployable architecture to fit within the rocket shroud. Leveraging JWST, our team quickly settled on a 36-segment primary mirror using lightweight hexagonal mirrors. A key challenge for this architecture is to achieve a 500 nm diffraction-limited performance, which allocates approximately 10-15 nm RMS of wavefront error (WFE) to thermal stability. This is nearly a factor of 5 times better than the JWST requirements, which employs a passive thermal architecture and a 14-day WFSC update of the primary mirror. For comparison, JWST uses lightweight composite structures, athermalized mounts and materials to assure the system is stable through observational slews to meet a 50 nm RMS allocation on thermal stabilityⁱⁱⁱ.

For ST-2020, dynamic disturbances (causing jitter) could be controlled with the use of technology developed for JWST for dynamic isolation, leaving the key challenge to be thermal stability. A solution to the temporal problem of thermal stability is more frequent updating of the segmented primary mirror alignment. This poses an additional challenge because slewing the observatory between fields of interest and a WFSC target star would be both

inefficient and by itself cause further instability. To solve this problem, our team has proposed a novel Hybrid Sensor Active Control (HSAC) architecture that combines the Fine Guidance Sensor (FGS), used to guide the telescope, and the wavefront sensor (WFS) into a single instrument that uses guide stars in the observatory field-of-view (FOV) to perform frequent updates to the telescope alignment.

ST-2020 MISSION CONCEPT

ST-2020 has been designed to be compatible with an EELV that would be a relatively modest upgrade of existing launch vehicles (LVs). Like JWST, ST-2020 would be launched into an orbit around the L2 Lagrange point that provides consistent full-sunlight, no temperature variations, and gives ST-2020 a constant field of regard (FOR) of about 3π steradians. A telescope in this orbit has roughly double the observational efficiency of a telescope in low Earth orbit (LEO), and is very stable thermally, which is important for controlling WFE.

As shown in Figure 1, ST-2020 employs an open baffle design with a planar, deployable sunshield. This sufficiently reduces stray light without requiring a fixed cylindrical light shield, such as used on HST. ST-2020 has a primary mirror consisting of 36 hexagonal segments coupled with an active WFSC system. This architecture permits the use of mirrors with low areal density, which in turn enables ST-2020 to make better use of the approximately 15,000-kg payload the EELV can put into orbit at L2.

In order to reduce dynamic disturbances by nearly a factor of 4 times over JWST, ST-2020 employs a Disturbance Isolator Precision Pointing System (DIPPS), which actively isolates the telescope from the spacecraft. This technology was initially proposed for JWST but requires additional development. ST-2020 also employs an actuated pointing arm (PA), which allows the OTA to be pointed at targets without changing the solid angle view of the sunshield with respect to the sun, a key source of instability on JWST. Together, these active isolation technologies assure that a 4x WFE improvement over JWST can be met. More importantly, since the active optical control occurs on a time scale of minutes, it can be accomplished without far more complex and expensive fast sensing and control such as a laser truss with a millisecond updates.

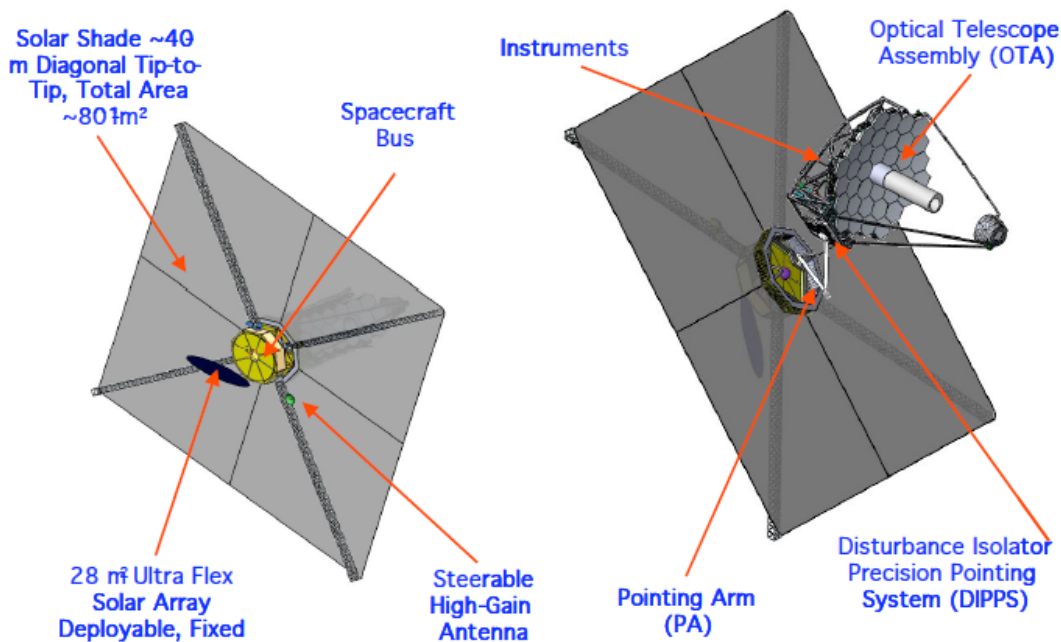


Figure 1 – ST-2020 spacecraft, OTA, and sunshield mission concept, as viewed from the bottom (left) and top (right).

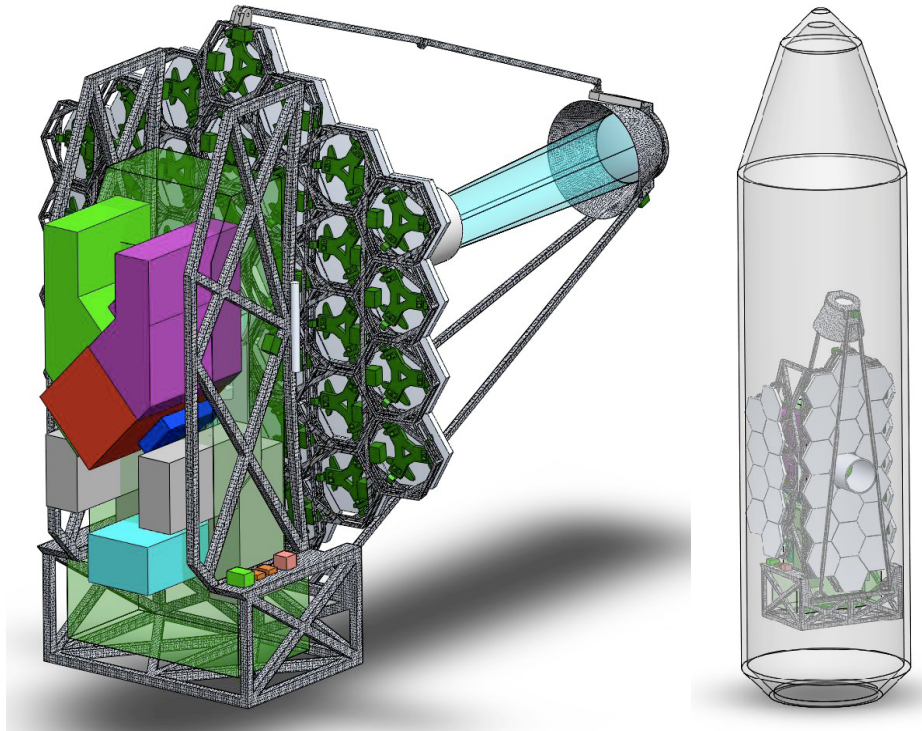


Figure 2 – Left: ST-2020 deployed OTA showing individual instrument packages mounted on the backplane structure. Right: retracted telescope in the EELV.

The OTA for the ST-2020 concept includes a 9.2-meter diameter, 36-segment primary mirror. The design employs both a 2-mirror Cassegrain channel for ultraviolet science and planet-finding instruments and a 4-mirror WFOV channel. The design leverages highly from the JWST telescope architecture with modifications to address the size and UV-optical performance. The deployable configuration consists of two wings (each wing contains 7 segments), a secondary mirror support structure, as well as a central baffle for controlling stray light. The primary mirror segments are held on a large composite backplane. The basic elements of this architecture are shown in Figure 2 and Figure 3.

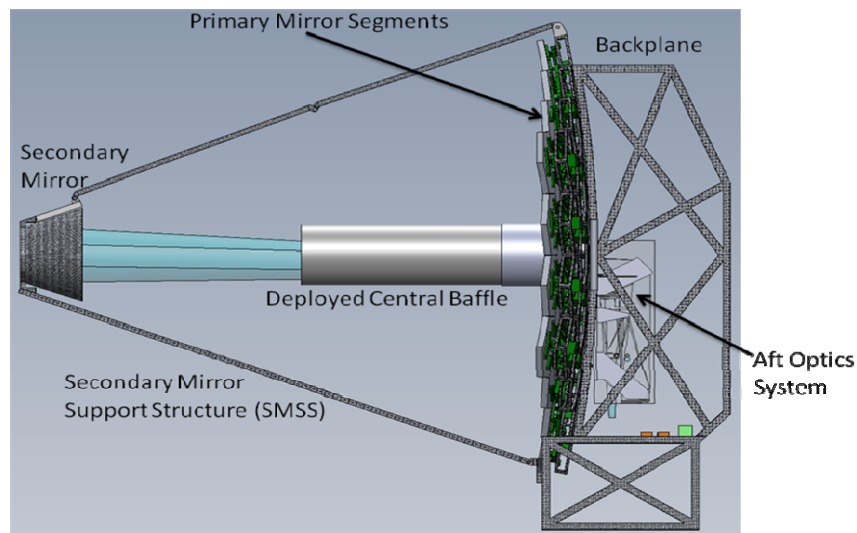


Figure 3 – ST-2020 deployed OTA. Instrument packages have been removed to show the aft optics system.

A new approach employed in the ST-2020 architecture is the use of an active WFSC architecture that updates the primary mirror every 5 to 30 minutes and updates the secondary mirror once a day. The active architecture replaces the passive thermal architecture of JWST, which updates the primary mirror every 14 days and the secondary mirror approximately once a year. This change was necessitated by the 500 nm diffraction-limit, which drove a factor of 4x improvement in the WFE requirement to 40 nm RMS. The WFE has been allocated to individual pieces of the architecture in the error budget in

Figure 4.

| | |
|----------------------------------|-----------------------|
| Diff. Lim. Wavelength (nm): | 490.7 |
| Top Level Error: | 40.9 ($\lambda/12$) |
| Top Level Error (nm RMS): | |
| OTA: | 34.5 |
| SI: | 22.0 |
| OTA (nm RMS): | |
| WFSC Residual: | 9.7 |
| Thermal Stability: | 10.0 |
| Image Motion: | 20.0 |
| OTA Static: | 24.4 |
| WFSC Residual (nm RMS): | |
| Sensing: | 9.5 |
| Control: | 2.0 |
| OTA Static (nm RMS): | |
| Design: | 13.0 |
| Align: | 10.0 |
| Figure: | 18.0 |
| Figure (nm RMS): | |
| PM: | 15.0 |
| SM: | 10.0 |

Figure 4 – Top-level wavefront error budget. All units are nanometers of RMS wavefront.

The mirror technology baselined for ST-2020 is a hexagonally shaped, 1.315-meter flat-to-flat, ultra-low expansion (ULE) mirror architecture initially proposed for JWST, with the understanding that ST-2020 would benefit from lighter, more active mirrors but that they are not critical to enabling the mission. One area requiring improvement over the AMSD and JWST ULE mirror concepts is better WFE performance and mirror matching. ULE was chosen as the baseline because UV-quality WFE has been demonstrated over smaller mirrors (including mid- and high-frequency performance), though improved edges are desirable. A summary of the key drivers for the ST-2020 mirror technology and how they compare to the AMSD ULE mirror is shown below in Figure 5. While a ULE mirror is the baseline, there are other ULE and Silicon Carbide based options that are either lighter weight and integrate active controls for removal of gravity sag or even figure. These options could prove attractive if they achieve acceptable WFE over the full power spectral density (PSD) and they are compatible from a system perspective.



Figure 5 – Left: AMSD mirror. Right: Comparison of ST-2020 and AMSD mirror requirements.

OPTICAL DESIGN

The optical configuration for ST-2020 consists of two basic channels, shown in Figure 6. The UV and extra-solar planetary instruments pick off the 2-mirror Cassegrain front end, which is coated with Al-MgF for superior UV throughput and is well corrected over the limited FOV required by the UV and extra-solar instruments. The wide field-of-view (WFOV) channel adds two more powered mirrors to the telescope to correct a larger annular FOV. The WFOV design essentially combines a Three Mirror Anastigmat (TMA) with a pupil corrector, where the Cassegrain portion of the TMA has been slightly optimized for the UV/optical channel. The WFOV optics are coated with silver which has a very high reflectivity over the WFOV wavelength range. Fold optics are used to inject the WFOV channel into the instruments. The FOV layout of the ST-2020 TMA instruments is shown in Figure 7.

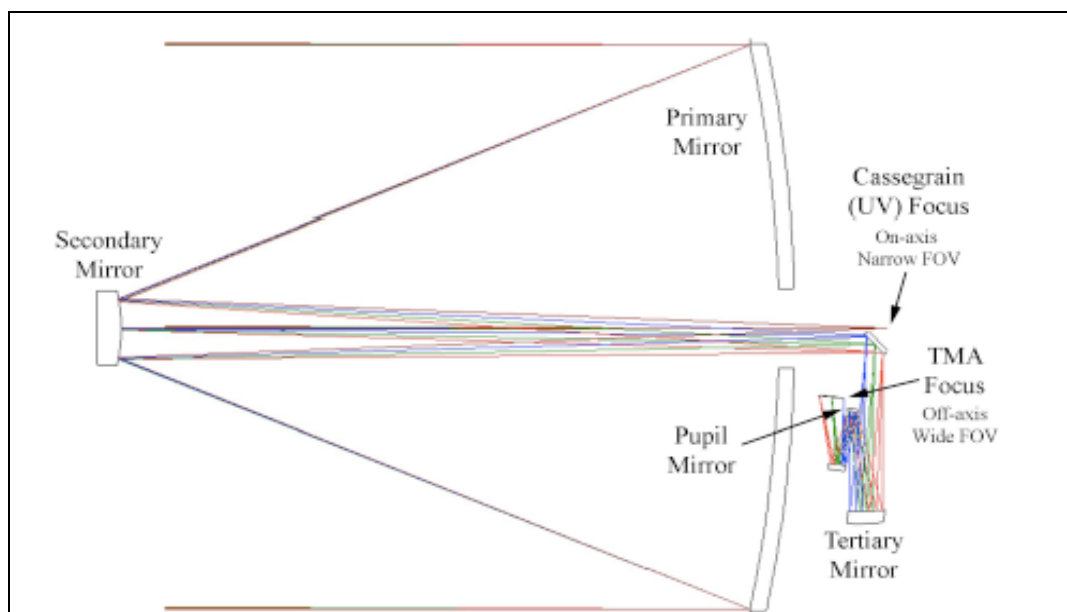


Figure 6 – Optical configuration for ST-2020.

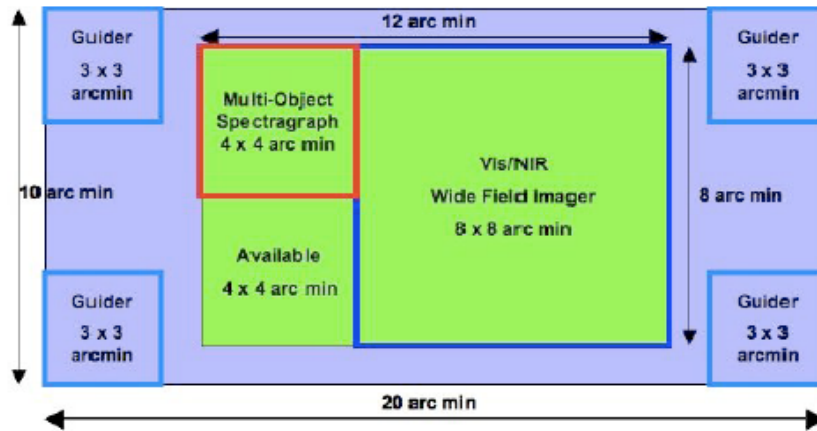


Figure 7 – Notional Field-of-view of the TMA focal plane. Hybrid “wavefront / fine-guidance” sensors occupy the 4-quadrants of the FOV

HYBRID WFS/FGS ARCHITECTURE

Guidance and wavefront sensing will be performed by a set of four, nearly identical instruments known as Hybrid Instruments (HI). Though the HIs draw heavily on technologies verified for JWST, development will be necessary to improve performance to meet the requirements of ST-2020.

A schematic of one of the HIs is shown in Figure 8 and a mechanical model is shown in Figure 9. Light from the OTA is fed to the HI via a pick-off mirror. A bi-directional star selection mirror (SSM) is used to access a 4×4 arcmin FOV and steer an isolated bright star onto the Fine Guidance Sensor (FGS) and Wavefront Sensing (WFS) detectors. The beam of light is split three ways, with 20% of the light going to the FGS detector for guidance and 40% of the light going to each of two WFS detectors. Each WFS detector is a $2k \times 2k$ CCD with $4.5 \mu\text{m}$ pixels. The FGS detector is a $2k \times 2k$ CCD with $12 \mu\text{m}$ pixels.

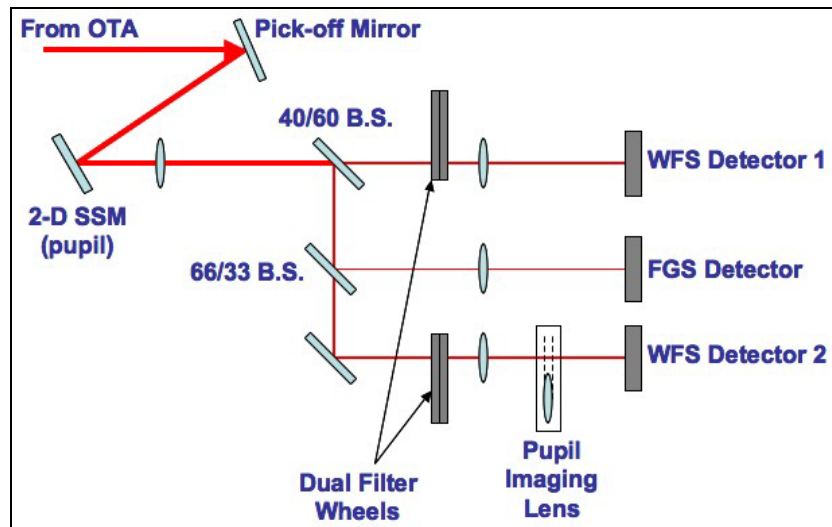


Figure 8 – Schematic of a Hybrid Instrument (HI).

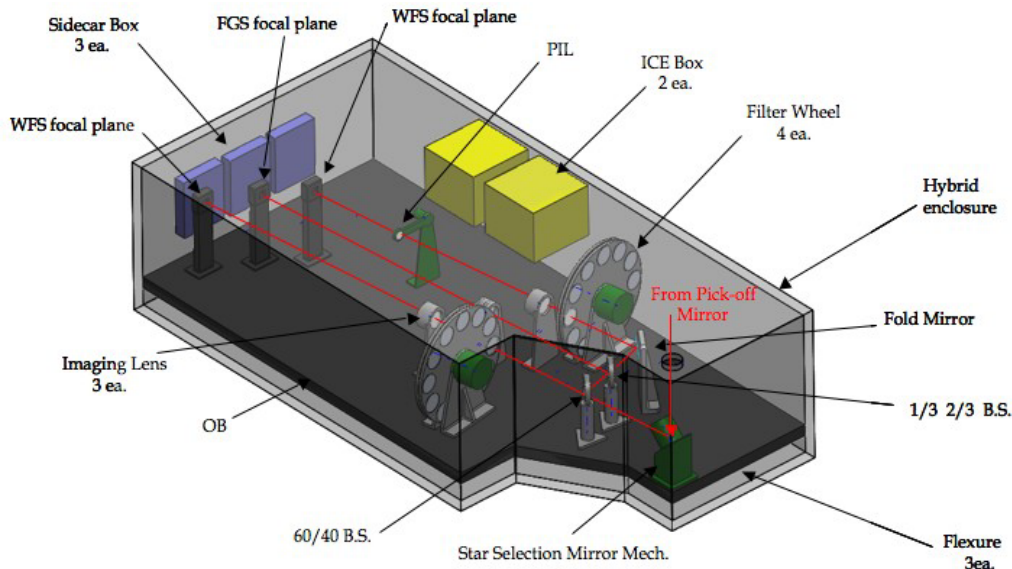


Figure 9 – Mechanical model of one of the HIs. Light from the pick-off mirror enters the instrument near the lower right of the drawing

The instantaneous FOV of each WFS detector is only 0.19×0.19 arc-minutes. The SSM allows that FOV to be extended to 4×4 arc-minutes while keeping the overall length of the system within reason. The optical design is a telecentric system, which helps remove uncertainty of the pupil amplitude and shape, and makes the WFS algorithm more robust.

The FGS beam path has only imaging optics to form a broadband image of the star on the detector for centroiding and guidance. Each WFS beam path contains a dual filter wheel and imaging optics to form a narrowband, out-of-focus image of the star on each of the WFS detectors. One of the two WFS beam paths will also contain an actuated pupil-imaging lens (PIL) that may be inserted to create an image of the OTA pupil on the detector.

Instrument Calibration:

Since each of the HIs is located near the edge of the FOV of the observatory (see Figure 7), the wavefront error is large compared to the on-axis wavefront error. This wavefront error uncertainty may degrade the performance of the WFS algorithm. Furthermore, each HI will have internal aberrations that are in non-common path with other instruments on the observatory.

Two additional components not shown in Figure 8 will be used to mitigate these problems. A focal surface of the OTA is located just after the pick-off mirror leading into each of the HIs. Near this focal surface is where a series of calibrating LEDs and point-diffraction interferometer (PDI) pinholes are to be mounted. The LEDs will be aimed towards the WFS detectors and provide point-like sources on which wavefront sensing can be performed. These LEDs are used to calibrate the aberrations of the HI itself, which are non-common path to other instruments on the observatory. A star aimed at the PDI pinhole will produce an interference pattern on the WFS detectors which can be used to determine low-order OTA aberrations due to the location of the HI near the edge of the FOV. Knowledge of these aberrations will be used in the wavefront-sensing algorithm to help meet the requirement on WFS for controlling mirror segments. After careful calibration on the ground, both the PDI and LED's can be helpful to establish changes from ground to on-orbit and thereafter.

Fine Guidance Sensor:

At any given time, two HIs are required for guiding ST-2020. In one HI, closed-loop centroiding will be performed to generate commands for the attitude control system and SSM. The second HI, looking at a field point well separated from the first, will be used to sense observatory roll.

Initially, a full $2k \times 2k$ frame will be captured and read-out. The location of the guide star in the frame is determined and the SSM is actuated to move the star to the center of the frame. A second full frame is captured and again the location of the guide star is determined. An $8 \text{ pixel} \times 8 \text{ pixel}$ window about the star is read and centroiding at 5 Hz is performed at a noise-equivalent angle of 0.57 milli-arc-seconds. The FGS and attitude control will maintain pointing to within 1.3 milli-arc-seconds of image motion.

WAVEFRONT SENSING AND CONTROL

For ST-2020, there will be three operating modes of WFSC: primary mirror (PM) maintenance, secondary mirror (SM) maintenance, and as a commissioning/diagnostic. The WFS algorithm is an iterative hybrid-diversity phase-retrieval algorithm similar to that being developed for the JWST^{iv}.

PM Maintenance:

The PM maintenance mode is completely automated and will occur approximately every 5 – 30 minutes, depending on the radiometric brightness of the source. In this mode, only a single HI is used for WFSC. The filter wheels are actuated to place a narrow band ($\Delta\lambda/\lambda \approx 1\% - 5\%$) spectral filter in each beam path, as well as a weak lens. One path will use a positive weak lens while the other uses a negative weak lens to produce two out-of-focus images of the star. The images are sent to an on-board processor where the phase-retrieval algorithm processes the data and segment-motion commands are generated. To achieve the 5 – 30 minute duty cycle, the phase-retrieval algorithm is implemented on dedicated, specialized parallel computing hardware^v. This mode will be used to meet the PM WFE requirement.

SM Maintenance:

The SM maintenance mode will also be automated, but will require the use of 3 of the HIs and will be performed nominally about once a day. In this mode, each HI captures two out-of-focus images from three different points in the telescope's FOV. All six images are sent to the on-board computer where multi-field phase retrieval is performed. In this mode, SM-motion commands are generated in addition to segment-motion commands.

This mode is required to remove possible wavefront ambiguities that may be introduced by SM motion. For example, a misplaced SM may introduce astigmatism, which is indistinguishable from astigmatism of the PM when sensed at a single field point. Sensing at multiple field points helps to remove this ambiguity.

Commissioning / Diagnostic:

As the name implies, the commissioning/diagnostic mode will be used only after the initial deployment of the observatory, or as a diagnostic mode should the observatory become misaligned. The mode is entirely manual, allowing all images collected by the HIs to be sent to a ground-based control center for further analysis. There are several steps involved in commissioning, as shown in Figure 10. The initial 4-steps after deployment (SM Focus Sweep through Segment-Image Array) involve identifying the point-spread functions (PSF) of each segment on the WFS detectors. Global alignment uses phase retrieval on spots from each segment to characterize each segment individually, as well as provide information for better SM placement. Image stacking then moves each PSF to the center of the array by tilting each segment in the PM. Coarse phasing uses dispersed Hartmann sensor (DHS) elements^{vi} in the filter wheels to sense and correct the piston errors between each segment to approximately 200 nm. The PM fine-phasing routine is similar to the PM maintenance routine and multi-field alignment is similar to the SM maintenance routine.

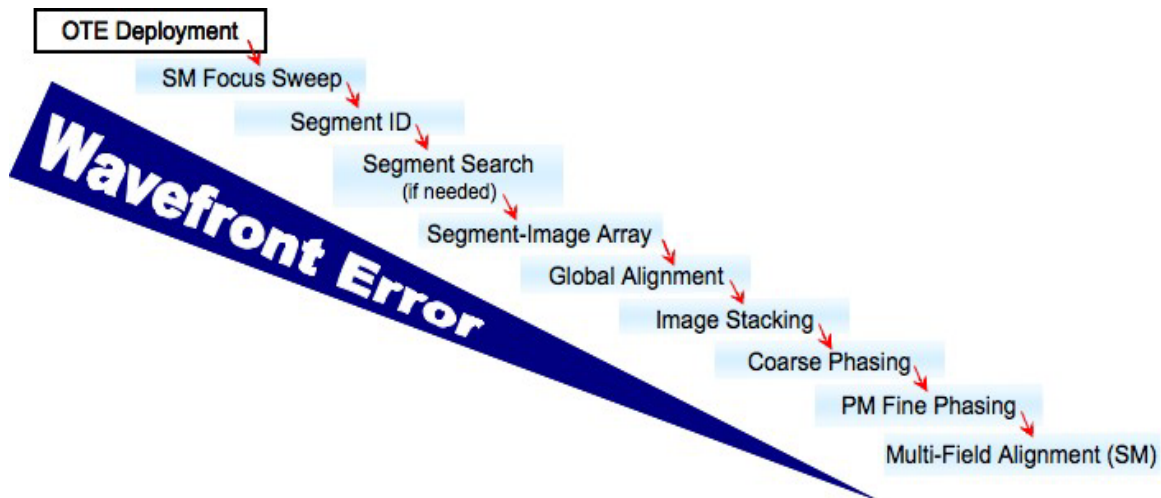


Figure 10 – Flow chart of the commissioning process

Also during commissioning, pupil images will be acquired using the PIL. The pupil images are used as Fourier constraints during the phase-retrieval processing of the data. Occasionally during the observatory's lifetime, updated pupil images will be required for diagnostic information or for updating the constraint used in the phase-retrieval processing.

WAVEFRONT SENSING & CONTROL SIGNAL-TO-NOISE

The planned update rate for WFSC maintenance operations is once every 5 – 30 minutes. This baseline sets requirements on factors such as algorithm speed, actuation and image integration time. The integration time for the defocused WFS images determines the signal-to-background ratio (SBR), defined as the ratio of the peak pixel value to the RMS of noise in a dark part of the image, hence, the SBR in turn affects the accuracy of the WFS algorithm. It is clear that the duty cycle of the WFSC system places a limitation on its ability to correctly align the PM segments and SM.

During typical observations, a bright star (relative magnitude < 15) will be used for WFSC PM maintenance. Under these conditions, out-of-focus PSFs will be captured using ± 8 waves or ± 10 waves of defocus, since it has been shown that larger amounts of defocus can give more accurate phase retrieval results at the target aberration spatial frequencies of interest^{vii}. Generally speaking, the target spatial frequencies are derived by considering the highest spatial frequency in the control system pass-band. In this scenario, wavefront estimates and PM segment commands can be generated approximately once every 5 minutes.

A trade is introduced when observing conditions are not ideal, for example when observing the North Galactic Pole (NGP) and only dim stars are available for WFS. Under these conditions, large amounts of defocus spread relatively few photons across a larger area on the detector, thus lowering the SBR. A lower SBR, in turn, results in larger errors in the wavefront estimated by the WFS algorithm. One must balance the amount of defocus to be large enough to tune the WFS algorithm to the desired aberration spatial frequencies, but small enough to maintain adequate SBR to estimate the controllable modes to the required accuracy. A study was performed to determine the trade-offs between source brightness, image defocus, and integration time, and how they affect SBR and therefore WFS accuracy.

For reference, Table 1 summarizes the availability of a given magnitude star being available in each of three HI FOVs at NGP (recall three HI's are necessary for SM Maintenance).

Table 1 – Probability of a given magnitude star being available in each of 3 Hybrid Instrument FOVs while observing the NGP.

| Star Magnitude | % Simultaneous Availability in 3 HI FOVs |
|----------------|--|
| 16 | 37.3 |
| 17 | 63.9 |
| 18 | 85.6 |
| 19 | 98.4 |
| 20 | 99.6 |

Next, a series of phase-retrieval simulations was performed to determine how the SBR would affect WFS for ST-2020. Table 2 shows the system parameters and assumptions used in the study. A larger number of realistic noise sources and uncertainties were included to accurately model how well phase retrieval would estimate PM segment misalignments for ST-2020.

Figure 11 shows the resulting RMS error in the recovered wavefront, broken down by aberration type, for two images defocused by ± 6 waves and different SBRs. The red dashed line represents the requirement for WFS on ST-2020 for the controllable modes of the PM, namely segment piston, tip and tilt. It is clear that the controllable modes can be sensed with the required accuracy for an SBR as small as 25.

A second portion of the study was aimed at determining what SBRs are achievable for a given relative magnitude star, integration time, and amount of defocus. Radiometric calculations related source brightness to the number of photons incident at the WFS detectors. Ten random wavefronts were used to simulate PSFs to determine how those photons were distributed on the detector so that SBRs could be calculated. Figure 12 shows average SBR calculations for a relative-magnitude 19 star, for different amounts of defocus as a function of integration time. Included in the Figure is a table outlining the minimum SBR required for each amount of defocus to achieve the required accuracy in sensing the controllable modes of the wavefront. Both ± 4 waves and ± 6 waves of defocus achieve the required minimum SBR for integration times of approximately 17 minutes and 27 minutes, respectively. Neither ± 8 or ± 10 waves of defocus meet the minimum SBR for integration times shorter than 30 minutes, but as discussed earlier, larger defocus settings are desired when increased resolution is necessary for trouble-shooting or maintenance operations.

Table 2 – System parameters and assumptions used for the phase-retrieval simulations.

| Parameter | Value |
|---|---|
| Wavelength | 500 nm \pm 12.5 nm (5% bandwidth, sampled by 5 wavelengths) |
| $Q = \lambda \times (F/\#) / \text{pixel size}$ | 2 |
| Diversity | { ± 4 , ± 6 , ± 8 , ± 10 } PV Waves Defocus |
| PSF Size | 512 \times 512 pixels |
| Unknown Wavefront Error | $\lambda/10$ RMS |
| Pupil Apodization Uncertainty | 6% |
| Pupil Amplitude Distortion Uncertainty | 0.1% |
| Charge Diffusion | 1.6% city block, 0.15% diagonal |
| Detector Quantization | 16 bits |
| Plate Scale Uncertainty | 0.1% |
| Jitter Uncertainty | 25% pixel symmetric |
| Pixel MTF | Over-sampled PSF by 3x |
| Dust | 3% PAC |
| Flat Field Uncertainty | 10% |

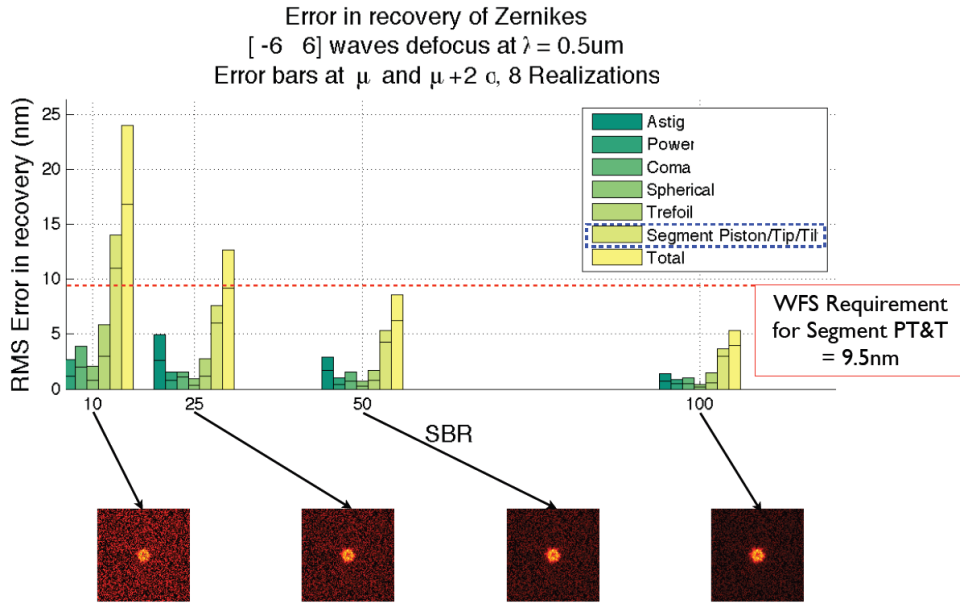


Figure 11 – RMS error in the estimated wavefront as a function of Signal-to-Background Ratio (SBR) for a pair of PSFs defocused by ± 6 waves. The red dashed line denotes the requirement on sensing the controllable modes of segment piston, tip and tilt.

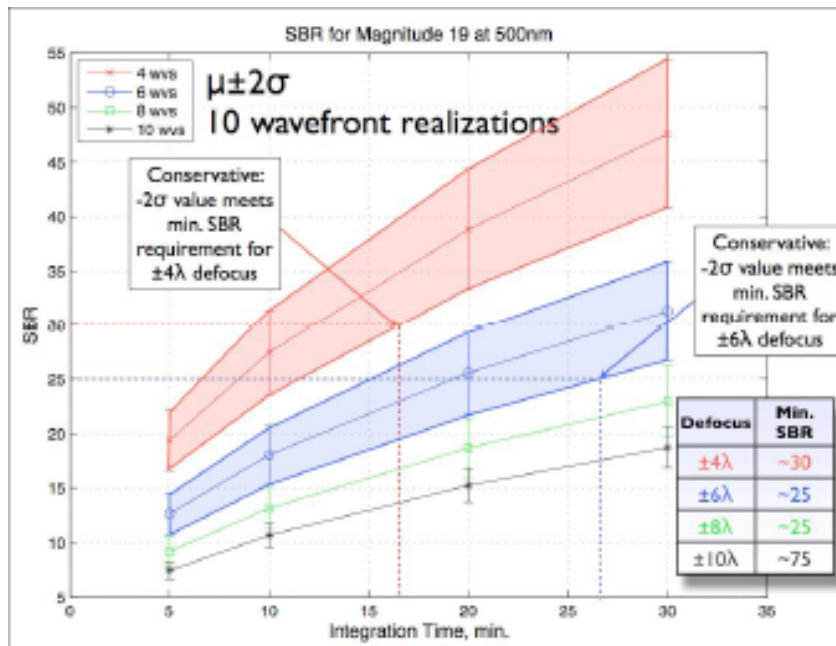


Figure 12 – SBR as a function of integration time for a relative-magnitude 19 star. The table on the right denotes the minimum SBR required for each amount of defocus to meet the WFS requirement on estimating the controllable modes.

SUMMARY

A novel hybrid approach to wavefront sensing and control and fine guidance sensing has enabled a cost-effective architecture for a large UV-optical telescope. This approach highly leverages the design of the James Webb Space Telescope. The architecture has inherent mass advantages over other approaches. The biggest limitation in the approach is the availability of guide stars in the north galactic pole, though we have demonstrated that this is a fairly minor limitation. The architecture is sufficiently general to be applicable to even larger telescopes although it requires a constant guide star in the field of view. The architecture forms the basis of the ST-2020 9.2 meter telescope architecture proposed as part of the ATLAST mission.

REFERENCES

- ⁱ Marc Postman et al, "Advanced Technology Large-Aperture Space Telescope (ATLAST): A Technology Roadmap for the Next Decade",
http://www.stsci.edu/institute/atlast/documents/ATLAST_NASA_ASMCS_Public_Report.pdf, May 2009
- ⁱⁱ H. P. Stahl, L. D. Feinberg, S.C. Texter, "JWST Primary Mirror Selection", Proc. SPIE 5487, pp. 818-824, (2004)
- ⁱⁱⁱ Paul Lightsey, Allison Barto, James Contreras, "Optical Performance of the James Webb Space Telescope", Proc. SPIE 5487, pp 825-832 (2004)
- ^{iv} B.H. Dean, D.L. Aronstein, J.S. Smith, R. Shiri, and D.S. Acton, "Phase retrieval algorithm for JWST Flight and Testbed Telescope," Proc. SPIE 6265, pp. 626511 (2006).
- ^v J.S. Smith, B. H. Dean, and S. Haghani. "Distributed computing architecture for image-based wavefront sensing and 2D FFTs," Proc. SPIE 6274, pp. 627421 (2006).
- ^{vi} M. Albanese, A. Wirth, A. Jankevics, T. Gonsiorowski, C. Ohara, F. Shi, M. Troy, G. Chanan, S. Acton, "Verification of the James Webb Space Telescope coarse phase sensor using the Keck Telescope," Proc. SPIE 6265 (2006).
- ^{vii} B.H. Dean and C.W. Bowers, "Diversity selection for phase-diverse phase retrieval," J. Opt. Soc. Am. A 20, 1490-1504 (2003).